Whole-cell modeling in yeast predicts compartment-specific proteome constraints that drive metabolic strategies

Ibrahim E. Elsemman[1,7,#], Angelica Rodriguez Prado[2,3,#], Pranas Grigaitis[2,#], Manuel Garcia Albornoz[4], Victoria Harman[5], Stephen W. Holman[5], Johan van Heerden[2], Frank J. Bruggeman[2], Mark M.M. Bisschops[3], Nikolaus Sonnenschein[1], Simon Hubbard[4], Rob Beynon[5], Pascale Daran-Lapujade[3], Jens Nielsen[1,6,*], and Bas Teusink[2,*]

[1] Novo Nordisk Foundation Center for Biosustainability, Technical University of Denmark, DK2800 Lyngby, Denmark

[2] Systems Biology Lab, Amsterdam Institute of Molecular and Life Sciences, Vrije Universiteit Amsterdam, The Netherlands

[3] Department of Industrial Microbiology, Technical University Delft, Delft, The Netherlands

[4] Division of Evolution & Genomic Sciences, University of Manchester, Manchester, UK

[5] Institute of Systems, Molecular and Integrative Biology, University of Liverpool, Liverpool, UK

[6] Department of Biology and Biological Engineering, Chalmers University of Technology, SE41296 Gothenburg, Sweden

[7] Current address: Department of Information Systems, Faculty of Computers and Information, Assiut University, Assiut, Egypt

[#] These authors contributed equally to this work

[*] To whom correspondence should be addressed: nielsenj@chalmers.se (JN), b.teusink@vu.nl (BT)

When conditions change, unicellular organisms rewire their metabolism to sustain cell maintenance and cellular growth. Such rewiring may be understood as resource re-allocation under cellular constraints. Eukaryal cells contain metabolically active organelles such as mitochondria, competing for cytosolic space and resources, and the nature of the relevant cellular constraints remain to be determined for such cells. Here we developed a comprehensive metabolic model of the yeast cell, based on its full metabolic reaction network extended with protein synthesis and degradation reactions (16304 reactions in total). The model predicts metabolic fluxes and corresponding protein expression by constraining compartment-specific protein pools and maximising growth rate. Comparing model predictions with quantitative experimental data revealed that under glucose limitation, a mitochondrial constraint limits growth at the onset of ethanol formation - known as the Crabtree effect. Under sugar excess, however, a constraint on total cytosolic volume dictates overflow metabolism. Our comprehensive model thus identifies condition-dependent and compartment-specific constraints that can explain metabolic strategies and protein expression profiles from growth rate optimization, providing a framework to understand metabolic adaptation in eukaryal cells.

Macromolecular synthesis and energy conservation by metabolism underlies cellular maintenance, growth and fitness. Unicellular organisms such as yeasts generally display a great variety of metabolic strategies that lead to competitive fitness across conditions[1]. The associated reprogramming of metabolism between such metabolic strategies is of key interest in biotechnology and biomedical research.

One well-known example is "overflow" metabolism in which under aerobic conditions not all substrate is fully oxidized but secreted as by-products. In cancer cells it is referred to as the Warburg effect: enhanced glycolytic activity with lactate as byproduct at the expense of respiration[2]. The same phenomenon is known as the Crabtree effect in *Saccharomyces cerevisiae* (Baker's yeast)[3]. At sugar limitation yeast respires glucose completely to CO_2; at sugar excess it displays respirofermentative metabolism, where respiration is combined with ethanol formation (alcoholic fermentation). The extent to which these two metabolic strategies are used can be titrated in a glucose-limited chemostat: at a specific "critical" dilution (=growth) rate, ethanol formation starts and increases linearly with growth rate[4]. Other microorganisms show similar behaviour[5]: for example, *E. coli* produces acetate at higher growth rates at the expense of respiration[6].

In the last decade a theoretical framework has been developed that can explain why cells shift metabolic strategies upon environmental or gene-expression perturbations[5,7–10]. In essence it is based on the catalytic benefits of proteins and their associated costs[11]. These costs comprise competition for resources such as building blocks, energy and synthesis machineries, and for space in cellular compartments. Two key features of this resource allocation paradigm can explain metabolic adaptations. First, cellular compartments can become "full" when they are fully occupied with (maximally) active proteins, such that an increase in one protein has to come at the expense of another. This was postulated as a phenomenological rule based on experimental observations[12], but also follows naturally from growth-rate maximization[13]. Second, cells allocate their limited resources for protein synthesis according to their demands[14,15]. Consequently, fractions of needed proteins vary with growth rate within

66 compartments whose protein content is bounded, and this can lead to "active proteome
67 constraints" related to full compartments.
68 Within this framework, the onset of overflow metabolism was explained by the smaller
69 protein cost of generating ATP through fermentation than respiratory pathways[6,7]; this becomes
70 important at fast growth when biosynthesis and ribosome demands are high and thus require
71 large proteome fractions. Earlier work suggests that the proteome-constrained resource
72 allocation paradigm, which was largely developed for *E. coli*, may also be a powerful perspective
73 for regulation of eukaryal yeast metabolism, such as ribosome biosynthesis[16], and growth on
74 different sugars[17]. However, a key feature of the metabolism of a eukaryal cell is the presence of
75 metabolically active organelles, most prominently mitochondria. Each organelle introduces two
76 new compartments (intra-organellar space and membrane), and how these compartments
77 impacts adaptation of metabolism, and which compartments become limiting under different
78 conditions, is an open question.
79 Moreover, despite the wealth of experimental data on *Saccharomyces cerevisiae*, a
80 comprehensive, quantitative, data set in which growth rate is systematically varied and both
81 fluxes and protein expression levels are measured, which are needed to validate resource
82 allocation predictions, are still rare (see however, some recent studies[16,18]). Here we generated
83 such data sets and in parallel developed the most detailed and comprehensive,
84 compartmentalized and quantitative model of metabolism and protein synthesis of yeast. The
85 model can compute the costs and benefits of protein expression and translocation; It can be used
86 to interpret or predict experimentally determined changes in growth rate, (minimal) protein
87 expression and metabolic fluxes as a result of growth rate optimization through resource
88 allocation into different, compartmentalized, proteome fractions. Comparison of the model
89 predictions with the data gives unprecedented insight into our physiological understanding of
90 this important model organism.
91

Results

Construction of a comprehensive proteome-constrained yeast model

We extended an existing[19] metabolic genome-scale metabolic model of yeast (GEM) by coupling metabolic fluxes to the synthesis of the catalysing enzyme and added constraints on protein concentrations, expressed as protein fractions of the total proteome (Fig. 1a). We refer to the resulting model as proteome-constrained Yeast (pcYeast). Earlier GEM-based approaches exist that incorporate resource allocation, and for yeast these considered constraints on enzyme activities and total protein content[17,20–23], whereas for *E. coli* constraints and reactions associated with transcription and translation were added[9]. Others considered membrane-area constraints and limitations of protein allocation to specific pathways[8,24]. We combined all these extensions (see Supplementary Notes for detailed information) to make pcYeast: a next-generation yeast GEM and computable knowledge base that incorporates protein expression, translation, folding, translocation and degradation at genome-scale for a compartmentalized, eukaryal, organism. In our current model, we consider the protein compartments most relevant for central metabolism: plasma membrane, cytosol, mitochondrion, and mitochondrial membrane. Other cell compartments such as the nucleus or endoplasmic reticulum are not (yet) specified explicitly - but do occupy volume in the cytosol.

The cellular proteome was divided into metabolically active, ribosomal, and unspecified (UP) proteins. The UP fraction is cytosolic, has an average amino acid composition and is added to always maintain a constant protein density in the cytosol. It has a minimum expression level estimated from the experimental proteomics data (Fig. S1, Supplementary Notes). The minimal UP fraction represents growth-rate independent structural, signalling and "household" proteins. Higher expression of UP than minimal represent both unspecified anticipatory proteins, or metabolic proteins that do not carry flux – including the unsaturated fraction of flux-carrying enzymes, as we will explain.

117 Metabolic enzymes are assigned to a specific compartment, either cytosol, plasma
118 membrane, mitochondrial matrix or inner mitochondrial membrane; Mitochondrial proteins
119 require additional protein transport complexes[25]. For each protein we comprehensively
120 modelled synthesis and degradation processes, which are responsible for the largest fraction of
121 cellular energy usage. Our model includes 1,523 proteins whose life cycles are described by
122 16,304 reactions that include translation initiation, elongation and termination factors,
123 ribosomal assembly factors, protein-specific folding by chaperones and degradation reactions,
124 as well as 5'UTR-length dependent energetic costs for translation initiation (Table 1,
125 Supplementary Notes).
126 We applied three classes of constraints that couple metabolic fluxes and peptides
127 synthesis rates (Fig. 1b and Supplementary Notes for details). The *enzyme capacity constraint*
128 sets the minimal enzyme synthesis rate required to achieve a certain metabolic flux. Thus, all
129 metabolically-active proteins are modeled to work at their maximal rate and are minimally
130 expressed in the model; the unsaturated fraction of flux-carrying enzymes is represented by UP,
131 the unspecified protein that is used to maintain protein density. In this way we prevent choices
132 about unknown regulatory and kinetic mechanisms that may affect the activity of enzymes;
133 rather we use the deviation between predicted minimal and measured actual protein expression
134 levels to indicate the level of saturation of each enzyme. The total enzyme synthesis rate is
135 constrained by the abundance of ribosomes through a *ribosome capacity constraint*, for both
136 cytosol and mitochondria. Finally, we added *compartment-specific constraints* on the proteome,
137 for the cytosol, the plasma membrane, and the mitochondrial matrix and inner membrane, (Fig.
138 1b). The values for these constraints are based on independent literature data or were fitted to
139 experimental data (as explicified in Supplementary Notes) and the values are either fixed or
140 growth-rate dependent, depending on the nature of the constraint.
141 The steady-state metabolite balances, the enzyme synthesis and degradation balances,
142 and the compartment-specific proteome constraints together specify a linear program with its
143 fluxes as optimisation variables, provided the growth rate is treated as a parameter. We use a

144 binary search algorithm to find the maximum growth rate where the linear program is still
145 feasible, and a marginal increase in the growth rate would result in an infeasible linear
146 programming problem. The model returns all the flux values associated with the maximal
147 feasible growth rate. It should be noted that the structure of the pcYeast model is strain-
148 independent: this allows subsequent calibration of the model to accommodate and account for
149 differences in cell physiology and metabolism, inherent to any specific strain of *S. cerevisiae*.
150

151 ## Calibrating the model against experimental data

152 We performed a series of experiments, using a wild-type *S. cerevisiae* strain CEN.PK 113-
153 7D, for collection of high-quality datasets of fluxes and protein levels, used either as model input
154 or for comparison with model predictions. We used glucose-limited continuous cultures
155 operated at dilution rates close to the critical dilution rate for ethanol formation, to capture
156 proteome change upon the onset of overflow metabolism. Additionally, we varied the growth
157 rate in pH-controlled batch experiments, either with different sugar quality or through
158 translation inhibition. We measured fluxes, including O_2 and CO_2 fluxes (Supplementary Dataset
159 1), which combined with biomass measurements, allowed to estimate the so-called maintenance
160 parameters, i.e. ATP usage that is not explicitly accounted for in the model (Supplementary
161 Notes). Label-free proteome quantification allowed us to reliably estimate proteome fractions of
162 around 3000 of the 6000 proteins (Supplementary Datasets 2, 3, and 4).
163 Parameters associated with translation strongly affected our model outcomes, and we
164 used published quantitative proteomics data[16] to estimate parameters for protein translation,
165 such as the elongation rate (Supplementary Notes). Following experimental reports we assumed
166 a constant inactive fraction of ribosomes and a fixed saturation of the actively translating
167 ribosomes[16,27] and were able to describe the growth-rate dependent ribosome mass fraction
168 with the model (Fig. 1c). As evidence for correctly capturing the costs of protein synthesis, we
169 correctly predicted the effect of over-expressing mCherry, an unneeded, "gratuitous" protein, on
170 the specific growth rate (Fig. 1d).

171

172 ## The model predicts shifts in metabolic strategies

173 We subsequently used the model to analyse yeast's physiological response to different
174 levels of glucose availability. Traditional Flux Balance Analysis computes continuous chemostat
175 cultures by minimizing glucose uptake rate at fixed growth (=dilution) rate[28]. Here we
176 simulated glucose availability by varying the degree of saturation of the glucose transporter. We
177 needed to constrain the maximal expression level of the glucose transport system based on
178 literature data (Supplementary Notes), as leaving expression free to occupy available membrane
179 space led to unrealistically high expression levels and overestimation of growth rate at low
180 glucose levels. At each saturation level we computed the maximal feasible growth rate and
181 compared model predictions with published data[29], and with data from our glucose-limited
182 chemostat cultures (growth rates between 0.2 – 0.34 h^{-1}). We also included our data from batch
183 cultures on glucose (growth rates 0.37-0.39 h^{-1}) and on trehalose; Trehalose is a disaccharide of
184 two glucose molecules, hydrolyzed extracelullarly[30], thus providing slow release of glucose that
185 supports low growth rates.

186 As in the chemostat the specific growth rate is equal to the dilution rate, the maximal
187 feasible growth rate that the model predicted can be directly compared to the experimental data
188 (Fig. 2a, 2c-d). The (residual) glucose concentrations were calculated from documented (high)
189 affinity of the transporters, which is close to 1 mM[31]. The resulting relationship between growth
190 rate and residual glucose concentration fit experimental data very well (Fig. 2a), validating our
191 expectation that we could ignore glucose efflux from the cells due to minute levels of
192 intracellular glucose[32] (see Supplementary Notes for details). Increasing glucose transporter
193 saturation increased predicted growth rate, and the effect saturated (Fig. 2b), suggesting that at
194 maximal growth rate further increase in glucose availability has little impact. Predicted biomass
195 yield (Fig. 2c) and fluxes (Fig. 2d) corresponded well with the experimental data, as did the
196 intracellular flux ratios from previously published ^{13}C-labeling flux analysis at three specific
197 growth rates in glucose-limited chemostat cultures (Supplementary Figure 2). In particular, the

198 model predicted a maximal oxygen consumption rate at dilution rates higher than 0.28 h^{-1}, at the
199 onset of ethanol formation. Above 0.35 h^{-1}, this rate rapidly drops to the low level that is
200 observed under glucose excess (batch) conditions. We conclude that the model can adequately
201 predict the changes in metabolic fluxes when the growth rate is varied through the availability of
202 glucose.
203

204 ## Changes in metabolic strategies are the result of proteome constraints

205 We used pcYeast to identify the active proteome constraints, *i.e.* the protein pools that
206 limit growth rate, because, according to resource allocation theory, the number of active
207 proteome constraints determines the maximal number of independent metabolic behaviors that
208 are possible in optimal states[5,13]. For this we computed the occupancy of each protein pool: a
209 pool that is fully occupied is indicative of an active constraint. At low growth rates, below 0.28 h^{-}
210 ^{1}, the glucose transporter was the only proteome pool that is fully occupied (Fig. 2e). With only
211 glucose uptake as active constraint, pure respiration is the single optimal strategy. At the onset
212 of ethanol formation a second metabolic mode started to carry flux (for formal computation of
213 these modes and the concomitant theory, see Supplementary Notes), and thus a second
214 constraint must have become active. Indeed, at this growth rate the occupancy of the inner-
215 mitochondrial membrane became maximal (Fig. 2e). Thus, the model suggests that under
216 glucose-limited chemostat conditions, the onset of ethanol formation is caused by a limit of the
217 mitochondrial membrane space, and hence the amount of proteins that yeast can maximally
218 express in this compartment.
219 At a growth rate of 0.35 h^{-1} we found that the unspecified protein level reached its
220 minimal value (Fig. 2e), equivalent to the cytosol being completely filled with maximally active
221 proteins. Further growth rate increase requires higher ribosomes and biosynthetic protein
222 fractions, which now has to come at the expense of the least proteome-efficient pathway. The
223 model confirmed earlier calculations[33] that respiration is less proteome efficient than
224 fermentation (Supplementary Figure 3) and respiration is therefore replaced by fermentation.

225 The model suggested therefore that at growth rate above 0.35 h^{-1} the second growth-limiting
226 constraint was shifted from the mitochondrial proteome to the cytosolic proteome. Thus, the
227 metabolic changes in the model, when growth rate and thus metabolic fluxes increase, are
228 dictated by the filling up of different cellular compartments with active protein, unique for an
229 eukaryal cell. The level of detail in our model to suggest the condition-dependent, active,
230 protein-concentration constraints belonging to different compartments has so far not been
231 provided by any other model.
232

233 ## Proteomics data validates model predictions

234 We subsequently measured protein levels with quantitative proteomics and compared
235 them to the minimal protein levels that the model predicted to be needed to support metabolic
236 flux. Since we compute minimal levels as if all the enzymes worked at their maximal rate, we
237 expected to underestimate most proteome fractions. Especially at lower growth rates where
238 nutrient limitation is most severe, one can expect lower average enzyme saturation, and indeed
239 we observed larger deviations between predicted minimal protein levels and measured protein
240 fractions at low growth rates (Fig. 3a). The difference between the predicted minimal level and
241 the data may be interpreted as a proxy for the average saturation of enzymes. In terms of
242 protein synthesis costs, the difference between the experimentally measured enzyme expression
243 and the predicted minimal expression level, however, are covered by the expression of the UP.
244 We see an overall tendency that the saturation of enzymes increases with growth rate
245 (Supplementary Figure 4). This is most prominent for the glycolytic pathway; also for amino
246 acid biosynthesis, the protein expression is higher than expected based on metabolic activity,
247 indicating also here a substantial undersaturation of the enzymes, as observed before for
248 bacteria such as *E. coli*[34] and *L. lactis*[35]. We find similar patterns for other biosynthetic pathways,
249 except for lipids (Supplementary Figure 5).
250 For mitochondrial proteins involved in the citric acid cycle and respiration, however, we
251 found that predicted minimal proteome fractions were very close to the measured ones (Fig.

252 3a). Unless k_{cat} values of mitochondrial enzymes are systematically underestimated, this
253 indicates that mitochondrial proteins work at higher average saturation than cytosolic proteins -
254 and seemingly close to their maximal capacity. Regardless of absolute numbers, the saturation of
255 the mitochondria seems rather constant, suggesting that yeast tunes the total amount of
256 mitochondria, rather than make excess (hence subsaturated) mitochondria, at least under these
257 conditions. This may make sense, given the extra costs of mitochondrial components such as
258 membranes, and for protein translocation of host-derived proteins during mitochondrial
259 biogenesis, which competes for membrane space with respiratory proteins.
260 Upon closer inspection, we observed that at the onset of ethanol formation the total
261 mitochondrial protein fraction started to decrease (Fig. 3b). The observed decay follows the
262 theoretical dilution-by-growth kinetics if at that point the rate of mitochondrial biosynthesis has
263 reached a maximum (Fig. 3b). Thus, the data suggests that the rate of mitochondrial biogenesis,
264 rather than the maximal mitochondrial membrane area currently used by the model, may reach
265 the host's maximal capacity at the onset of ethanol formation. When we zoom in on the
266 mitochondrial proteome, we find that the mitochondrial ribosome fraction increased as a
267 funtion of growth rate, and also other proteins re-allocated (Supplementary Fig. 6). Indeed,
268 mitochondria are self-replicating entities abiding to the same resource allocation principles as
269 the host, which even includes selection for fast replication - but obviously severely dictated by
270 the proteins the host provides. More data related to the mitochondrial biosynthetic processes,
271 such as mitochondrial ribosomal capacity and protein import machinery would be required to
272 predict the maximal mitochondrial growth rate from first principles, which is outside the scope
273 of this study. Nonetheless, the distinct changes of mitochondrial proteins at the critical dilution
274 rate are consistent with the model prediction that a mitochondrial constraint is responsible for
275 the onset of ethanol formation under glucose-limited conditions.
276

Constraints and fluxes under sugar excess conditions

We then varied growth rate (between 0.05 h^{-1} and 0.4 h^{-1}) by providing different sugars, i.e. trehalose, galactose, maltose and glucose during batch cultivation. Ethanol production was already observed on galactose, already at a growth rate of 0.16 h^{-1} so at a much lower growth rate than the critical growth rate of 0.28 h^{-1} under glucose-limited growth (Fig. 4a). Maltose showed intermediate growth rate and fluxes. Initial model simulations with a "naïve" model using the reported catalytic rates of the transporters and catabolic enzymes involved in galactose and maltose metabolism, however, resulted in predicted growth rates and fluxes not far from growth on glucose. This suggests that there are additional cost factors that were not included in the model, and or that *Saccharomyces cerevisiae* is not as well adapted to these sugars.

We therefore used the model as data analysis tool to estimate possible changes in parameters that fit the observed growth rate and corresponding fluxes (see Supplementary Notes for details). Such parameter changes may be interpreted as costs for suboptimal metabolism of carbon sources other than glucose. The onset of ethanol formation at a growth rate of 0.16 h^{-1} required a combination of changes in both sugar uptake and the intracellular proteome (through the minimal UP fraction constraint): a lower sugar uptake capacity alone would be identical to lowering saturation of the transporter as was done for glucose (Fig. 2), and pure respiration would have been found at 0.16 h^{-1}. Conversely, only an increase in minimal UP would have resulted in a proportional flux decrease that we also found with mCherry overexpression (or translation inhibition, Supplementary Figure 7), and more ethanol were to be found.

We had to decrease the maximal galactose uptake rate by a factor of 2.5 compared to glucose. Furthermore, an increase in minimal UP fraction was needed, to 0.49 g/g protein. To fit all fluxes optimally, we also required additional energetic costs (see Supplementary Notes), whose mechanistic underpinning remains to be explored but may be related to the reported toxicity of galactose intermediates[36]. Such a change in energetic costs were not needed to

304 describe the data for growth on maltose: only a change in the maltose uptake rate and minimal
305 UP fraction (of 0.34 g/g protein) were required to achieve good fit.
306 For maltose, a disaccharide of glucose, the reason for the required parameter changes is
307 not clear. Only a maltose proton-symporter and a maltase protein distinguishes it from growth
308 on glucose. The transport expression may be tightly regulated as very high maltose uptake rates
309 can result in substrate-accelerated death[37]. For galactose, the toxicity of its intermediates[36]
310 results in an evolutionary trade-off with growth on glucose[38]; on galactose yeast cells appear to
311 be still prepared for growth on glucose, which may prevent them from optimal expression of
312 proteins on galactose, as shown by expression titration experiments[39]. Indeed, laboratory
313 evolution experiments on galactose select mutations in Ras/cAMP signalling and adapted strains
314 show increased growth rates and concomitant increased ethanol fluxes[38]. Interestingly, the
315 direction of change points to the optimal behaviour predicted by the initial naïve model,
316 suggesting that the pcYeast model may aid in predicting the direction of evolutionary change
317 during laboratory evolution experiments (Supplementary Figure 8).
318 With the updated parameters, we identified for both sugars that the active constraints
319 limiting growth were the sugar transport expression and the minimal UP fraction constraint
320 (Figure 4d, Supplementary Notes, Supplementary Figure 9). These active constraints explains
321 ethanol formation during growth on galactose even though the growth rate is lower than the
322 critical dilution rate on glucose.
323

324 ## Proteomics data on sugar excess shows re-allocation of metabolic strategies

325 If growth rate is actively constrained by the cytosolic proteome under galactose, maltose
326 and glucose excess conditions, it implies that all cytosolic proteins work at their maximum
327 activity, and changes in flux must be brought about by changes in protein level. We therefore
328 turned to proteomics again. Comparing the minimal levels of the model with experimental data,
329 we find again that mitochondrial proteins for the TCA cycle and respiration are very similar to
330 the predicted minimal levels required to sustain flux (Fig. 4c). Cytosolic proteins were

331 underestimated - even at sugar excess conditions. (Note however that the expected maximal
332 attainable activity is not likely at the maximal rate in the forward direction as product inhibition
333 is inevitable in a chain of enzymes.)

334 More indicative of "a full cytosol" is that at the onset of ethanol formation (at galactose
335 growth rate and higher) we find evidence for proportional relationships between protein and
336 flux for high-flux carrying, pathway-grouped, proteins as a function of growth rate (Fig. 4c). This
337 is observed even down to the individual protein level (also involving changes in expressed
338 isozymes), as illustrated for glycolytic and respiratory proteins in Fig. 4d. This implies that
339 under these conditions, enzyme saturation was constant (and maximal, we expect) and changes
340 in flux could only be brought about by corresponding changes in enzyme levels. This data
341 illustrates how mitochondrial proteins are being traded in for glycolytic proteins needed for an
342 enhanced fermentation and growth rate. It also confirms the model's prediction that the
343 cytosolic proteome constraint is active during growth on these sugars.

344

345 Inhibition of translation highlights the role of environmental signalling in coordination 346 of metabolism in yeast.

347 Finally we varied growth rate by translation inhibition by cyclohexamide under
348 controlled glucose batch conditions, and again measured fluxes, growth rate and proteome
349 profiles (Fig. 5a). Upon inhibition of translation, we found a decrease in growth rate and close to
350 proportional decreases in glucose, ethanol and CO_2 fluxes, for both the model and the
351 experimental data (Fig. 5b). Such behaviour is expected when one dominant constraint is active
352 and its extent is varied (cf. glucose-limited fully respiratory growth, Fig. 2). In the case of glucose
353 excess, the model suggested that the cytoplasmic volume was fully occupied with active proteins
354 (minimal UP constraint was hit), and inhibition of translation required higher expression levels
355 of ribosomes, taking away limited proteome space for growth-supporting activities.

356 However, experimental observations compromised this initial explanation. First, for
357 oxygen the model also predicted a proportional increase with growth rate, but experimentally

358 the fluxes did not change much as did the expression of enzymes involved in oxygen
359 consumption, such as TCA cycle and oxidative phosphorylation (Fig. 5d). Moreover, the
360 ribosomal proteome fraction increased much less with inhibition than the model predicted (Fig.
361 5c). Since translation inhibition in the model has the same effect as overexpression of a non-
362 functional protein (Supplementary Figure 7), we followed the earlier observation that the
363 inactive fraction of ribosomes could be recruited for translation, depending on the translational
364 load[16], with only a small improvement (Supplementary Figure 10).
365 This suggested that either some constraint prevents the ribosomal fraction from
366 increasing to the optimal levels predicted by the model, or the expression of ribosomes in yeast
367 is dominantly regulated by environmental nutrient signalling and less by internal cues. A
368 dominant role of signalling in ribosomal biogenesis has been suggested before[16]. In yeast the
369 TOR pathway appears to be the master regulator of ribosomal biosynthesis and assembly at
370 steady-state growth[40,41]. Following the TOR-specific targets described by Kunkel[41], we find that
371 key target proteins of this signalling pathway, including ribosomal auxiliary factors, had
372 constant expression levels (Supplementary Figure 11 and Supplementary Table 1), supporting
373 the dominant role of external rather than internal cues.
374 When we constrained ribosomal expression to the measured maximal response,
375 ribosomal expression rapidly became the only active constraint in the model, and the proteome
376 space that became available in the cytosol at the lower growth rates was used for increased
377 respiration (Supplementary Figure 12). This is not observed experimentally, and our data
378 suggest that respiration does not respond to internal cues either. In contrast the fluxes and
379 expression of proteins involved in glycolysis and amino acid metabolism did decrease with
380 growth rate (Fig. 5bd). This suggests that these pathways must be sensitive to internal feedback
381 regulation, as is well known for amino acid metabolism[42]. Thus, the proportional fluxes we found
382 for ethanol and glucose upon translation inhibition, are likely the result of control by demand[43],
383 with lower demand at lower growth rate.
384

385 ## Discussion

386 In this work, we developed the most comprehensive model of a growing,
387 compartmentalized, eukaryal cell to date. It includes all its known metabolic reactions, and
388 details of the protein synthesis, degradation and transport machinery to express the enzymes.
389 The key of our approach is the application of constraints on protein pools in the different
390 compartments that have direct biochemical meaning and could be independently estimated
391 from literature data. Our approach is unique in level of detail and in dealing with cellular
392 compartmentation, in particular of the mitochondria. We furthermore generated a unique set of
393 high-quality quantitative data on both fluxes and the proteome under different, well-controlled,
394 conditions. Through integration and comparison with the model, we provide deeper insight into
395 the physiology of *Saccharomyces cerevisiae*.

396 First, we firmly established that metabolic growth strategies of yeast on glucose can be
397 well understood from a proteome-constrained optimisation problem with growth rate as
398 objective. Through our high resolution sampling around the critical dilution rate, we observed
399 distinct changes in proteins exactly at the onset of ethanol formation in the glucose-limited
400 chemostat. We also show that the active constraints that drive these changes can be different
401 under different conditions such as batch growth on galactose - even if ethanol is made in both
402 cases. Our approach to identify the active cellular constraints may resolve some of the
403 discussion in current literature about *the* cause of overflow metabolism, not only in yeast but
404 possibly also in other eukaryotes, including discussion about the Warburg effect in mammalian
405 cells[44].

406 Second, the proteome constraints of the model are currently based on experimental
407 observations, but further research could drill deeper into their origin. For example, why would
408 the protein density in the cytosol be relatively constant? Does this balance diffusion rates with
409 catalytic capacities[45]? Are the current morphological dimensions of a yeast cell optimal for
410 growth rate? Recent work on selection for cell number showed that smaller cells can be readily
411 selected for[46]. We also identified that the levels of glucose transport and that of mitochondria

412 need to be constrained to describe the data. Why would yeast not express these components at
413 higher levels? In the case of mitochondria, the proteomics data suggest that rather than a
414 maximum mitochondrial membrane area and matrix volume, there is a maximal rate of
415 mitochondrial biogenesis. Can we calculate this rate from first principles? One could imagine
416 that an upper limit for mitochondrial "growth rate" exists if all but eight metabolic proteins need
417 to be transported over the same membrane that must also harbour the full machinery for
418 oxidative phosphorylation. Moreover, we focused on mitochondrial protein content, and ignored
419 details on morphology, lipid synthesis, or possible assembly costs. Thus, a next version of the
420 model will need to address the mitochondrial transport, biosynthesis and morphology in much
421 more detail.

422 In the case of glucose transport, the model suggested that further increase in glucose
423 transporters beyond wild type expression did not increase growth rate substantially and would
424 likely be invisible for evolution. At maximal saturation of the transporter, glucose transport
425 expression was (just) no longer an active constraint in our model (Fig. 2e). Thus, it appears as if
426 yeast expresses just enough glucose transporters to maximise its growth rate under glucose
427 excess – as found in bacteria[47]. Expressing higher transport levels at lower glucose levels would
428 enhance growth rate but may not pay off if this state is a transient towards glucose starvation, or
429 could be outright dangerous if suddenly glucose would become available[37]. The expression level
430 of the hexose transporters may thus have evolved to be an adaptation to dynamic
431 environments[48]. Long-term evolution experiments in glucose-limited chemostats indeed show
432 gene duplications of high-affinity glucose transporters[49], showing that growth limitation, and
433 hence selection pressure, is on glucose transport under these conditions.

434 Third, in the case of nutrient uptake limitation, there appears to be "excess" proteome
435 space that could be filled with anticipatory proteins or heterologous enzymes at no cost in
436 fitness. Even though the composition of such excess proteome space cannot be predicted with
437 our model, we were able to predict metabolic fluxes very well: in this nutrient-limited regime
438 metabolic efficiency (ATP per glucose), not proteome efficiency (ATP per protein), determines

439 the best growth rate strategy. This explains why Flux Balance Analysis applied to only the
440 metabolic network has been so successful, but only under nutrient-limited conditions.
441 Finally, we found linear or even proportional relationships between growth rate and
442 flux, and between flux and enzyme levels in a sugar excess (batch culture) regime. In terms of
443 regulation analysis[50], such a regime is characterised by hierarchical regulation with absence of
444 metabolic regulation, that is, all changes in flux are brought about by changes in enzyme levels,
445 not their degree of saturation. For glycolysis and amino acid metabolism, the average saturation,
446 estimated as the ratio of the predicted minimal enzyme level to the expressed enzyme level, at
447 maximal growth rate is around 0.5, incidently the level predicted as theoretical optimum for
448 specific reaction rate[51]. In contrast, when growth is limited by glucose availability, the degree of
449 saturation varies and the model suggests a mixture of hierarchical and metabolic regulation, as
450 previously observed in chemostats as well[52].
451 To conclude, we present a mechanistic, compartmentalized, model of an eukaryal
452 organism in full details, which can act as a valuable, computable, knowledge base. We show how
453 it can be used to compute protein costs and identify active growth-limiting constraints, and how
454 it can be combined with quantitative flux and proteomics data to provide unprecedented insight
455 into cellular physiology. Finally, we show that also in eukaryal cells, metabolic strategies can be
456 understood on the basis of growth rate optimisation under nutrient and proteome constraints.
457 What remains to be understood is how the cell's signalling and regulatory networks manage to
458 implement these (optimal) proteome allocation strategies.
459

460 # Methods

461 **Model development**

462 The full description of the pcYeast model is provided as Supplementary Notes. The model codes
463 are available per request to the authors and will be published on GitHub upon acceptance of this
464 manuscript.

465

466 **Strains and shake flask cultivation**

467 The strain used for this study was *Saccharomyces cerevisiae* strain CEN.PK 113-7D[53]. The stocks
468 used for the experiments were grown in 500 mL shake flask containing 100 mL of YPD medium
469 (10 g L^{-1} of Bacto yeast extract, 20 g L^{-1} of peptone and 20 g L^{-1} of D-glucose). The culture was
470 grown up to early stationary phase and 1 mL aliquots were stored in 20% (v/v) of glycerol at -
471 80 °C. For chemostats, pre-cultures were grown in 500 mL shake flasks containing 100 mL of
472 synthetic medium, the pH was set to 6.0 with 2M KOH and the medium was supplemented with
473 20 g L^{-1} of D-glucose[54]. Shake flasks with medium were inoculated with the 1 mL frozen stocks of
474 the strain and the cultivations were performed in an orbital shaker at 200 rpm at 30 °C. Pre-
475 cultures for batches with translation inhibitors were performed using a similar approach,
476 whereas for batches with different carbon sources the pre-cultures were made with the
477 respective carbon sources instead of D-glucose.

478

479 **Chemostat cultivations**

480 Chemostat cultivations were performed in 2 L bioreactors (Applikon, Schiedam, The
481 Netherlands) with a working volume of 1.0 L, the dilution rates used in this study were 0.2, 0.23,
482 0.27, 0.3, 0.32 and 0.34 h^{-1} in two independent replicate cultures. Growth rates were controlled
483 by modifying the inflow rate on each experiment. Synthetic medium according to Verduyn[54]
484 supplemented with 7.5 g L^{-1} of glucose and 0.25 g L^{-1} Pluronic 6100 PE antifoaming agent was
485 supplied to the bioreactor from a 20 L continuously mixed reservoir vessel. Cultures were
486 sparged with dried air at a flow rate of 700 mL min^{-1} and stirred at 800 rpm. The pH of the
487 cultures was maintained at 5.0 by automatic addition of 2 M KOH. If, after at least six volume
488 changes, the cultures dry cell weight concentration and carbon dioxide production ratediffered
489 less than 2% over two consecutive volume changes the cultures were considered to be in steady
490 state. For cultures with dilution rates of 0.27, 0.3, 0.32 and 0.34 h^{-1}, cultures were first

491 maintained at a dilution rate of 0.2 h^{-1} for 15 hours (3 volume changes) prior to increasing the
492 specific dilution rate to said values.
493
494 **Batch cultivations with different carbon sources**
495 Batch cultivations (two independent replicate cultures) were performed using synthetic
496 medium[54], the medium was supplemented with 20 g L^{-1} final concentrations of the carbon
497 sources, either D-trehalose, D-galactose, D-maltose or D-glucose (Sigma Aldrich). The
498 bioreactors were inoculated with 100 mL of yeast shake flask cultures, exponentially growing on
499 the specific carbon source. The final OD_{660} of all pre-cultures was 4. Cultivations were performed
500 at 30 °C, the pH was kept at 5.0 by automatic addition of 2M KOH. The working volume of the
501 bioreactors was 1.4 L in 2 L bioreactors (Applikon, Schiedam, The Netherlands). The cultures
502 were stirred at 8000 rpm and sparged with a flow rate of 700 mL min^{-1} of dried air. Oxygen
503 levels were kept above 40% of the initial saturation level as measured with Clark electrode
504 (Mettler Toledo, Greifensee, Switzerland).
505
506 **Batch cultivations with the translation inhibitor cycloheximide**
507 Batch cultivations (two independent replicate cultures) with the translation inhibitor
508 cycloheximide were performed as for the batches with different carbon sources, except that all
509 the batch cultures ran on 20 g L^{-1} of D-glucose and were supplemented with different
510 concentrations of cycloheximide with the aim of reaching specific growth rates. In total five
511 growth rates were studied, being 0.06, 0.12, 0.2, 0.32 and 0.41 h^{-1} (adding respective
512 cycloheximide concentrations of 228.96, 124.51, 52.15, 25.99 and 0 µg L^{-1}).
513
514 **Analytical methods**
515 Cultures dry weight was measured by filtering 20 mL of culture, the sample was filtered in pre-
516 dried and pre-weight membrane filters with a pore size of 0.45 µm (Gelman Science), the filter

517 was washed with demineralized water, subsequently it was dried in a microwave (20 min, 350
518 W) and the final weight was measured as described previously.
519 For the measurement of organic acids and residual carbon source concentrations, supernatants
520 of the cultures were used. For carbon-limited chemostat cultures, the samples were directly
521 quenched with cold steel beads and filtered[55], whereas samples from batch cultures were
522 centrifuged (5 min at 16.000× g). The supernatants were analysed by high-performance
523 chromatography analysis on an Agilent 1100 HPLC (Agilent Technologies) equipped with an
524 Aminex HPX-87H ion-exchange column (BioRad, Veenendaal, The Netherlands), operated with 5
525 mM H_2SO_4 as the mobile phase at a flow rate of 0.6 mL min^{-1} and at 60 °C. Detection was
526 according to a dual-wavelength absorbance detector (Agilent G1314A) and a refractive-index
527 detector (Agilent G1362A), as described previously.
528 The exhaust gas from batch cultures was cooled down with a condenser (2°C) and dried with a
529 PermaPure Dryer (model MD 110-8P-4; Inacom Instruments, Veenendaal, the Netherlands)
530 before online analysis of carbon dioxide and oxygen with a Rosemount NGA 2000 Analyser
531 (Baar, Switzerland).
532
533 **Glycogen and trehalose assays**
534 1 mL of culture was taken from the chemostats and directly added to 5 mL of cold methanol (-40
535 °C). The sample was mixed and centrifuged (4400× g, -20 °C for 5 minutes), the supernatant
536 was discarded, and the pellet was washed in 5 mL of cold methanol (-40 °C), and pellets were
537 stored at -80 °C until further processing. Subsequently, the pellets were resuspended in 0.25 M
538 Na_2CO_3 and processed as described previously[56,57]. D-glucose released from trehalose and
539 glycogen were measured with a D-glucose assay kit (K-GLUC Megazyme), two biological
540 replicates and three technical replicates were analysed per condition.
541
542 **RNA determination**

543 For RNA determination, 1-2 mL of broth was transferred to a filter (pore size of 0.45 µm, Gelman
544 Science), after which the filter was washed with cold TCA 5 %. The cells were resuspended in 3
545 mL of TCA 5% and centrifuged for 15 minutes at 4 °C at 4000 rpm. The supernatant was
546 removed and the pellet was stored at -20 °C. Finally, samples were processed as described by
547 Popolo et al., 1982. Two biological replicates and three technical replicates were analysed per
548 condition.
549
550 **Protein determination**
551 For the batches with CHX, culture volumes corresponding to 50 mg of DCW were centrifuged,
552 washed twice with cold demineralized sterile waterand divided into two aliquots of 5 mL. 2 mL
553 of the aliquot (containing 10 mg DW) was mixed with 1 mL of 3 M NaOH and incubated at 100 °C
554 for 10 minutes. The final mix was diluted and processed following the copper-sulfate based
555 method as described previously[58]. The absorbance of the supernatant was measured at 510 nm,
556 for calibration lyophilized bovine serum albumin (A2153, Sigma Aldrich) was used. Two
557 biological replicates and 3 technical replicates were analysed per condition.
558
559 **Proteomics sample preprocessing**
560 Aliquots of 20 mL of culture from chemostats and batches with different carbon sources were
561 centrifuged (4000 rpm 4 °C, 10 minutes) and washed two times, the final pellet was flash frozen
562 in liquid nitrogen and stored at -80 °C. Two biological replicates and two technical replicates
563 were analysed per condition.
564 Frozen cell pellets were thawed on ice before transfer to Precellys® Lysing Kit 2 ml screw cap
565 vials with 0.5mm glass beads (Bertin Instruments, France). Lysis was performed in 250 µl lysis
566 buffer, 50 mM ammonium bicarbonate with cOmplete protease inhibitor cocktail (ROCHE,
567 Switzerland), using a Minilys Personal Tissue Homogenizer (Bertin Instruments, France), at
568 maximum speed for 15 cycles of 30 seconds with a one-minute rest on ice between each cycle.

569 Lysed material was centrifuged for 10 minutes 13,000× *g* at 4°C, the supernatant fraction was
570 removed and retained. Fresh lysis buffer (250 µl) was added to the insoluble material, which
571 was resuspended before extraction from the vial via a small hole inserted into the vial base.
572 Soluble and insoluble fractions were recombined and the total final volume recorded. Protein
573 concentration was determined using Pierce™ Coomassie Plus Bradford Assay Kit (ThermoFisher
574 Scientific, UK).
575 Protein (100 µg) from each sample was treated with 0.05 % (w/v) RapiGest™ SF surfactant
576 (Waters, UK) at 80 °C for 10 minutes, reduced with 4 mM dithiothreitol (Melford Laboratories
577 Ltd., UK) at 60 °C for 10 minutes and subsequently alkylated with 14 mM iodoacetamide
578 (SIGMA, UK) at room temperature for 30 minutes. Proteins were digested with 2 µg Trypsin
579 Gold, Mass Spectrometry Grade (Promega, US) at 37 °C for 4 hours before a top-up of a further 2
580 µg trypsin and incubation at 37 °C overnight. Digests were acidified by addition of trifluoroacetic
581 acid (Greyhound Chromatography and Allied Chemicals, UK) to a final concentration of 0.5 %
582 (v/v) and incubated at 37 °C for 45 minutes before centrifugation at 13,000× *g* (4°C) to remove
583 insoluble non-peptidic material.
584
585 **Proteomics analytics**
586 The sample running order was randomised using a random number generator (Random.org).
587 Samples were analysed using an UltiMate™ 3000 RSLCnano system (ThermoFisher Scientific)
588 coupled to a Q Exactive™ HF Hybrid Quadrupole-Orbitrap™ Mass Spectrometer. Protein digests
589 (1 ug of each) were loaded onto a trapping column (Acclaim PepMap 100 C18, 75 µm x 2 cm, 3
590 µm packing material, 100 Å) using 0.1 % (v/v) trifluoroacetic acid, 2 % (v/v) acetonitrile in
591 water at a flow rate of 12 µL min-1 for 7 min.
592 The peptides were eluted onto the analytical column (EASY-Spray PepMap RSLC C18, 75 µm x
593 50 cm, 2 µm packing material, 100 Å) at 40°C using a linear gradient of 120 minute shallow
594 gradient rising from 8 % (v/v) acetonitrile/0.1 % (v/v) formic acid (Fisher Scientific, UK) to 30
595 % (v/v) acetonitrile/0.1 % (v/v) formic acid at a flow rate of 300 nL min^{-1}. The column was then

596 washed at 1 % A : 99 % B for 8 min, and re-equilibrated to starting conditions. The nano-liquid
597 chromatograph was operated under the control of Dionex Chromatography MS Link 2.14.
598 The nano-electrospray ionisation source was operated in positive polarity under the control of
599 QExactive HF Tune (version 2.5.0.2042), with a spray voltage of 2.1 kV and a capillary
600 temperature of 250°C. The mass spectrometer was operated in data-dependent acquisition
601 mode. Full MS survey scans between m/z 300-2000 were acquired at a mass resolution of
602 60,000 (full width at half maximum at m/z 200). For MS, the automatic gain control target was
603 set to $3e^6$, and the maximum injection time was 100 ms. The 16 most intense precursor ions
604 with charge states of 2-5 were selected for MS/MS with an isolation window of 2 m/z units.
605 Product ion spectra were recorded between m/z 200-2000 at a mass resolution of 30,000 (full
606 width at half maximum at m/z 200). For MS/MS, the automatic gain control target was set to
607 $1e^5$, and the maximum injection time was 45 ms. Higher-energy collisional dissociation was
608 performed to fragment the selected precursor ions using a normalised collision energy of 30 %.
609 Dynamic exclusion was set to 30 s.
610
611 **Proteomics data analysis**
612 The resulting raw data files generated by XCalibur (version 3.1) were processed using MaxQuant
613 software (version 1.6.0.16)[59]. The search parameters were set as follows: label free experiment
614 with default settings; cleaving enzyme trypsin with 2 missed cleavages; Orbitrap instrument
615 with default parameters; variable modifications: oxidation (M) and Acetyl (protein N-term); first
616 search as default; in global parameters, the software was directed to the FASTA file; for
617 advanced identification "Match between runs" was checked; for protein quantification we only
618 used unique, unmodified peptides. All other MaxQuant settings were kept as default. The false
619 discovery rate (FDR) for accepted peptide spectrum matches and protein matches was set to
620 1%. The CEN.PK113-7D Yeast FASTA file was downloaded from the *Saccharomyces* Genome
621 Database (SGD) (https://downloads.yeastgenome.org/sequence/strains/CEN.PK/CEN.PK113-
622 7D/CEN.PK113-7D_Delft_2012_AEHG00000000/).

The resulting MaxQuant output was then analysed using the MSstats package (version 3.5.6)[60] in the R environment (version 3.3.3) to obtain differential expression fold changes with associated *p* values, along with normalized LFQ and intensity values as described previously[61].

Acknowledgements

This work was supported by NWO (NWO ERA-IB-2, project No 053.80.722 to BT and PDL), ERA-IB 4207-00002B DSForsk to JN, and Biotechnology and Biological Sciences Research Council (BB/M025748/1 to S. Hubbard, BB/M025756/1 to RB). PG and BT also acknowledge support by Marie Skłodowska-Curie Actions ITN "SynCrop" (grant agreement No 764591). We thank SURFsara for the HPC resources through access to the Lisa Compute Cluster.

Author Contributions

Conceptualization, funding acquisition and supervision: BT, JN, PDL, RB, S. Hubbard; experimental data collection: ARP, VH, S. Holman; experimental data analysis: ARP, PG, MGA, MMMB; computational modeling: IEE, PG; formal analysis: IEE, PG, JvH, FJB, NS, JN, PDL, BT; writing – original draft: BT; writing – editing: IEE, PG, FJB, JN, BT. All authors have read and approved the manuscript.

References

1. Blank, L., Lehmbeck, F. & Sauer, U. Metabolic-flux and network analysis in fourteen hemiascomycetous yeasts. *FEMS Yeast Res.* **5**, 545–558 (2005).
2. Pfeiffer, T. & Morley, A. An evolutionary perspective on the Crabtree effect. *Front. Mol. Biosci.* **1**, 1–6 (2014).
3. De Deken, R. H. The Crabtree effect: a regulatory system in yeast. *J. Gen. Microbiol.* **44**, 149–156 (1966).

648 4. Van Hoek, P., Van Dijken, J. P. & Pronk, J. T. Effect of specific growth rate on fermentative
649 capacity of baker's yeast. *Appl. Environ. Microbiol.* **64**, 4226–4233 (1998).
650 5. de Groot, D. H., van Boxtel, C., Planqué, R., Bruggeman, F. J. & Teusink, B. The number of
651 active metabolic pathways is bounded by the number of cellular constraints at maximal
652 metabolic rates. *PLOS Comput. Biol.* **15**, e1006858 (2019).
653 6. Basan, M. *et al.* Overflow metabolism in Escherichia coli results from efficient proteome
654 allocation. *Nature* **528**, 99–104 (2015).
655 7. Molenaar, D., van Berlo, R., de Ridder, D. & Teusink, B. Shifts in growth strategies reflect
656 tradeoffs in cellular economics. *Mol. Syst. Biol.* **5**, 323 (2009).
657 8. Mori, M., Hwa, T., Martin, O. C., De Martino, A. & Marinari, E. Constrained Allocation Flux
658 Balance Analysis. *PLoS Comput. Biol.* **12**, 1–24 (2016).
659 9. O'Brien, E. J., Lerman, J. A., Chang, R. L., Hyduke, D. R. & Palsson, B. Genome-scale models of
660 metabolism and gene expression extend and refine growth phenotype prediction. *Mol. Syst.*
661 *Biol.* **9**, (2013).
662 10. Scott, M., Gunderson, C. W., Mateescu, E. M., Zhang, Z. & Hwa, T. Interdependence of Cell
663 Growth and Gene Expression: Origins and Consequences. *Science* **330**, 1099–1102 (2010).
664 11. Wortel, M. T., Bosdriesz, E., Teusink, B. & Bruggeman, F. J. Evolutionary pressures on
665 microbial metabolic strategies in the chemostat. *Sci. Rep.* **6**, 29503 (2016).
666 12. Scott, M. & Hwa, T. Bacterial growth laws and their applications. *Curr. Opin. Biotechnol.* **22**,
667 559–565 (2011).
668 13. Wortel, M. T., Peters, H., Hulshof, J., Teusink, B. & Bruggeman, F. J. Metabolic states with
669 maximal specific rate carry flux through an elementary flux mode. *FEBS J.* **281**, 1547–1555
670 (2014).
671 14. Berkhout, J. *et al.* How biochemical constraints of cellular growth shape evolutionary
672 adaptations in metabolism. *Genetics* **194**, 505–512 (2013).

673 15. Bosdriesz, E., Molenaar, D., Teusink, B. & Bruggeman, F. J. How fast-growing bacteria
674 robustly tune their ribosome concentration to approximate growth-rate maximization. *FEBS*
675 *J.* **282**, 2029–2044 (2015).
676 16. Metzl-Raz, E. *et al.* Principles of cellular resource allocation revealed by condition-dependent
677 proteome profiling. *eLife* **6**, e28034 (2017).
678 17. Sánchez, B. J. *et al.* Improving the phenotype predictions of a yeast genome-scale metabolic
679 model by incorporating enzymatic constraints. *Mol. Syst. Biol.* **13**, 935 (2017).
680 18. Björkeroth, J. *et al.* Proteome reallocation from amino acid biosynthesis to ribosomes
681 enables yeast to grow faster in rich media. *Proc. Natl. Acad. Sci.* **117**, 21804–21812 (2020).
682 19. Sánchez, B. J., Feiran Li, Hongzhong Lu, Kerkhoven, E. & Nielsen, J. *SysBioChalmers/yeast-*
683 *GEM: yeast 7.6.0*. (Zenodo, 2016). doi:10.5281/ZENODO.1495468.
684 20. Beg, Q. K. *et al.* Intracellular crowding defines the mode and sequence of substrate uptake by
685 Escherichia coli and constrains its metabolic activity. *Proc. Natl. Acad. Sci.* **104**, 12663–
686 12668 (2007).
687 21. Adadi, R., Volkmer, B., Milo, R., Heinemann, M. & Shlomi, T. Prediction of microbial growth
688 rate versus biomass yield by a metabolic network with kinetic parameters. *PLoS Comput.*
689 *Biol.* **8**, (2012).
690 22. Labhsetwar, P. *et al.* Population FBA predicts metabolic phenotypes in yeast. *PLOS Comput.*
691 *Biol.* **13**, e1005728 (2017).
692 23. Nilsson, A. & Nielsen, J. Metabolic Trade-offs in Yeast are Caused by F1F0-ATP synthase. *Sci.*
693 *Rep.* **6**, 22264 (2016).
694 24. Zhuang, K., Vemuri, G. N. & Mahadevan, R. Economics of membrane occupancy and respiro-
695 fermentation. *Mol. Syst. Biol.* **7**, 1–9 (2011).
696 25. Okamoto, K. The protein import motor of mitochondria: a targeted molecular ratchet driving
697 unfolding and translocation. *EMBO J.* **21**, 3659–3671 (2002).
698 26. Kafri, M., Metzl-Raz, E., Jona, G. & Barkai, N. The Cost of Protein Production. *Cell Rep.* **14**, 22–
699 31 (2016).

700 27. Bruggeman, F. J., Planqué, R., Molenaar, D. & Teusink, B. Searching for principles of microbial
701 physiology. *FEMS Microbiol. Rev.* **44**, 821–844 (2020).
702 28. Famili, I., Forster, J., Nielsen, J. & Palsson, B. O. Saccharomyces cerevisiae phenotypes can be
703 predicted by using constraint-based analysis of a genome-scale reconstructed metabolic
704 network. *Proc. Natl. Acad. Sci.* **100**, 13134–13139 (2003).
705 29. Canelas, A. B., Ras, C., ten Pierick, A., van Gulik, W. M. & Heijnen, J. J. An in vivo data-driven
706 framework for classification and quantification of enzyme kinetics and determination of
707 apparent thermodynamic data. *Metab. Eng.* **13**, 294–306 (2011).
708 30. Jules, M., Guillou, V., François, J. & Parrou, J.-L. Two distinct pathways for trehalose
709 assimilation in the yeast Saccharomyces cerevisiae. *Appl. Environ. Microbiol.* **70**, 2771–2778
710 (2004).
711 31. Diderich, J. A. *et al.* Glucose uptake kinetics and transcription of HXT genes in chemostat
712 cultures of Saccharomyces cerevisiae. *J. Biol. Chem.* **274**, 15350–15359 (1999).
713 32. Teusink, B., Diderich, J. A., Westerhoff, H. V., van Dam, K. & Walsh, M. C. Intracellular Glucose
714 Concentration in Derepressed Yeast Cells Consuming Glucose Is High Enough To Reduce the
715 Glucose Transport Rate by 50%. *J. Bacteriol.* **180**, 556–562 (1998).
716 33. Chen, Y. & Nielsen, J. Energy metabolism controls phenotypes by protein efficiency and
717 allocation. *Proc. Natl. Acad. Sci.* **116**, 17592–17597 (2019).
718 34. O'Brien, E. J., Utrilla, J. & Palsson, B. O. Quantification and Classification of E. coli Proteome
719 Utilization and Unused Protein Costs across Environments. *PLOS Comput. Biol.* **12**,
720 e1004998 (2016).
721 35. Goel, A. *et al.* Protein costs do not explain evolution of metabolic strategies and regulation of
722 ribosomal content: does protein investment explain an anaerobic bacterial Crabtree effect?:
723 Protein costs and evolution of metabolic strategies. *Mol. Microbiol.* **97**, 77–92 (2015).
724 36. de Jongh, W. A. *et al.* The roles of galactitol, galactose-1-phosphate, and phosphoglucomutase
725 in galactose-induced toxicity in *Saccharomyces cerevisiae*. *Biotechnol. Bioeng.* **101**, 317–326
726 (2008).

727 37. Postma, E., Verduyn, C., Kuiper, A., Scheffers, W. A. & Van Dijken, J. P. Substrate-accelerated
728 death ofSaccharomyces cerevisiae CBS 8066 under maltose stress. *Yeast* **6**, 149–158 (1990).
729 38. Hong, K.-K., Vongsangnak, W., Vemuri, G. N. & Nielsen, J. Unravelling evolutionary strategies
730 of yeast for improving galactose utilization through integrated systems level analysis. *Proc.*
731 *Natl. Acad. Sci. U. S. A.* **108**, 12179–12184 (2011).
732 39. Keren, L. *et al.* Massively Parallel Interrogation of the Effects of Gene Expression Levels on
733 Fitness. *Cell* **166**, 1282-1294.e18 (2016).
734 40. Chaker-Margot, M. Assembly of the small ribosomal subunit in yeast: mechanism and
735 regulation. *RNA* **24**, 881–891 (2018).
736 41. Kunkel, J., Luo, X. & Capaldi, A. P. Integrated TORC1 and PKA signalling control the temporal
737 activation of glucose-induced gene expression in yeast. *Nat. Commun.* **10**, 3558 (2019).
738 42. Chubukov, V., Gerosa, L., Kochanowski, K. & Sauer, U. Coordination of microbial metabolism.
739 *Nat. Rev. Microbiol.* **12**, 327–340 (2014).
740 43. Hofmeyr, J. S. & Cornish-Bowden, A. Regulating the cellular economy of supply and demand.
741 *FEBS Lett.* **476**, 47–51 (2000).
742 44. Vander Heiden, M. G. & DeBerardinis, R. J. Understanding the Intersections between
743 Metabolism and Cancer Biology. *Cell* **168**, 657–669 (2017).
744 45. Dill, K. A., Ghosh, K. & Schmit, J. D. Physical limits of cells and proteomes. *Proc. Natl. Acad. Sci.*
745 **108**, 17876–17882 (2011).
746 46. van Tatenhove-Pel, R. J. *et al.* Serial propagation in water-in-oil emulsions selects for
747 Saccharomyces cerevisiae strains with a reduced cell size or an increased biomass yield on
748 glucose. *Metab. Eng.* **64**, 1–14 (2021).
749 47. Jensen, P. R., Michelsen, O. & Westerhoff, H. V. Control analysis of the dependence of
750 Escherichia coli physiology on the H(+)-ATPase. *Proc. Natl. Acad. Sci.* **90**, 8068–8072
751 (1993).

752 48. Buziol, S. *et al.* Dynamic response of the expression of hxt1, hxt5 and hxt7 transport proteins
753 in Saccharomyces cerevisiae to perturbations in the extracellular glucose concentration. *J.*
754 *Biotechnol.* **134**, 203–210 (2008).
755 49. Gresham, D. *et al.* The Repertoire and Dynamics of Evolutionary Adaptations to Controlled
756 Nutrient-Limited Environments in Yeast. *PLoS Genet.* **4**, e1000303 (2008).
757 50. ter Kuile, B. H. & Westerhoff, H. V. Transcriptome meets metabolome: hierarchical and
758 metabolic regulation of the glycolytic pathway. *FEBS Lett.* **500**, 169–171 (2001).
759 51. Cornish-Bowden, A. The effect of natural selection on enzymic catalysis. *J. Mol. Biol.* **101**, 1–9
760 (1976).
761 52. Daran-Lapujade, P. *et al.* The fluxes through glycolytic enzymes in Saccharomyces cerevisiae
762 are predominantly regulated at posttranscriptional levels. *Proc. Natl. Acad. Sci.* **104**, 15753–
763 15758 (2007).
764 53. Nijkamp, J. F. *et al.* De novo sequencing, assembly and analysis of the genome of the
765 laboratory strain Saccharomyces cerevisiae CEN.PK113-7D, a model for modern industrial
766 biotechnology. *Microb. Cell Factories* **11**, 36 (2012).
767 54. Verduyn, C., Postma, E., Scheffers, W. A. & Van Dijken, J. P. Effect of benzoic acid on metabolic
768 fluxes in yeasts: A continuous-culture study on the regulation of respiration and alcoholic
769 fermentation. *Yeast* **8**, 501–517 (1992).
770 55. Mashego, M. R., van Gulik, W. M., Vinke, J. L. & Heijnen, J. J. Critical evaluation of sampling
771 techniques for residual glucose determination in carbon-limited chemostat culture
772 ofSaccharomyces cerevisiae. *Biotechnol. Bioeng.* **83**, 395–399 (2003).
773 56. Parrou, J. L., Teste, M.-A. & François, J. Effects of various types of stress on the metabolism of
774 reserve carbohydrates in Saccharomyces cerevisiae: genetic evidence for a stress-induced
775 recycling of glycogen and trehalose. *Microbiology* **143**, 1891–1900 (1997).
776 57. Boer, V., Daran, J., Almering, M., Dewinde, J. & Pronk, J. Contribution of the transcriptional
777 regulator Leu3p to physiology and gene expression in nitrogen- and carbon-limited
778 chemostat cultures. *FEMS Yeast Res.* **5**, 885–897 (2005).

58. Verduyn, C., Postma, E., Scheffers, W. A. & van Dijken, J. P. Physiology of Saccharomyces Cerevisiae in Anaerobic Glucose-Limited Chemostat Culturesx. *J. Gen. Microbiol.* **136**, 395–403 (1990).
59. Tyanova, S., Temu, T. & Cox, J. The MaxQuant computational platform for mass spectrometry-based shotgun proteomics. *Nat. Protoc.* **11**, 2301–2319 (2016).
60. Choi, M. *et al.* MSstats: an R package for statistical analysis of quantitative mass spectrometry-based proteomic experiments. *Bioinformatics* **30**, 2524–2526 (2014).
61. Garcia-Albornoz, M. *et al.* A proteome-integrated, carbon source dependent genetic regulatory network in *Saccharomyces cerevisiae*. *Mol. Omics* **16**, 59–72 (2020).

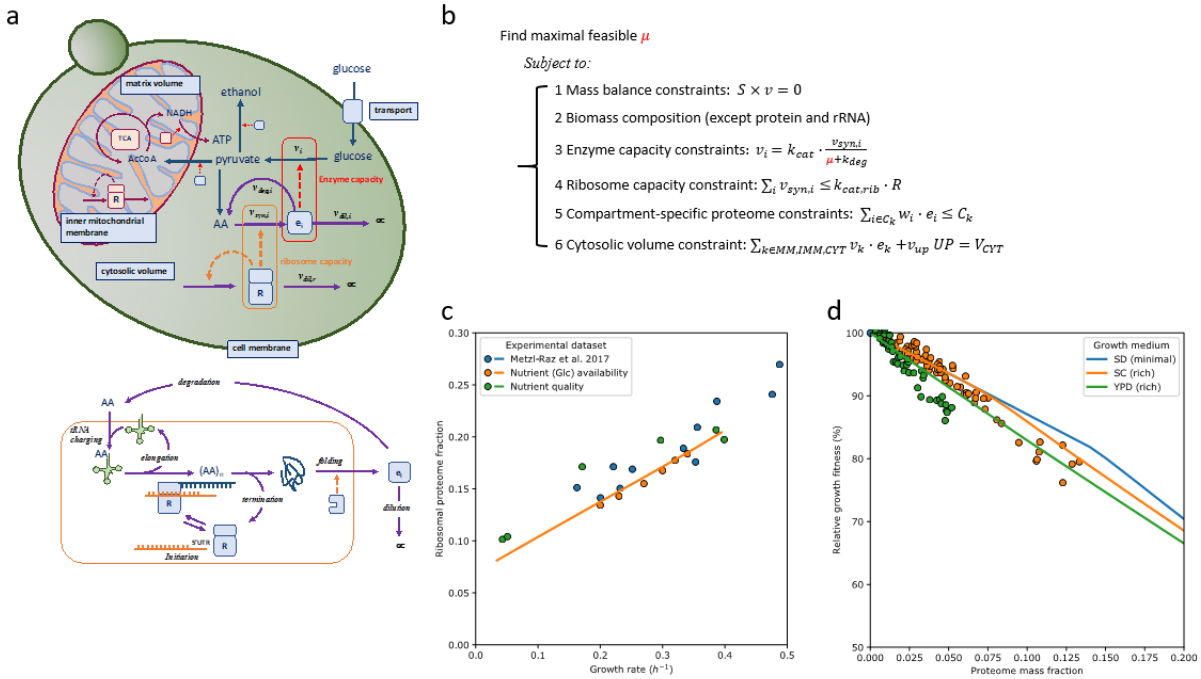

Fig. 1 pcYeast model formulation and calibration of protein synthesis parameters. **a.** A schematic overview of reactions in the model, their interdependence and constraints. Metabolic reactions v_i are proportional to enzyme concentrations e_i that are synthesized at rate $v_{syn,i}$ by the ribosomes R. Each protein can be degraded with rate $v_{deg,i} = k_{deg} \cdot e_i$ or diluted by growth rate $v_{dil,i} = \mu \cdot e_i$. Compartment-specific constraints are indicated in the light-blue boxes. **b.** Optimisation problem with the key constraints, including 1) steady-state mass balances; 2) production of biomass components such as DNA, lipids, cell wall and polysaccharides. Proteins and tRNA are excluded as their synthesis rates are optimisation variables 3) enzyme capacity constraints that couple metabolic flux to catalytic rate $k_{cat,i}$ and the enzyme level, whose value at steady state is determined by its synthesis rate, rates of enzyme degradation, and dilution by growth. Note we use equalities and hence enzymes work at their maximal rate and minimal required protein levels are computed; 4) ribosome capacity that defines an upper bound for protein synthesis rate; 5) compartment-specific proteome constraints that define the maximal concentration of proteins that can be contained in that compartment, with w_i the specific volume or area of protein i; 6) a cytosolic protein density constraint that has the same function as that of proteome constraints, but whose equality forces the cell to fill up any vacant

806 proteome space with unspecified protein UP with average amino acid composition. **c.** Growth rate was
807 varied through sugar type (trehalose, galactose, maltose, glucose) or glucose concentration, and
808 ribosomal protein fraction was determined by proteomics (which was consistent with literature data,
809 also plotted). The translation rate was calibrated on that data, as detailed in Supplementary Notes. **d.**
810 Impact of mCherry protein overexpression on growth rate. Symbols show experimental data[26], solid
811 lines show model predictions based on glucose minimal (SD) medium or rich SC/YPD media. Model
812 predictions were obtained by varying the proteome mass fraction, occupied by mCherry, and
813 determining the maximal predicted growth rate at each value of the mass fraction. The relative
814 growth fitness represents the ratio between the growth rate at certain mCherry expression level vs.
815 the unperturbed state (no mCherry expression).
816

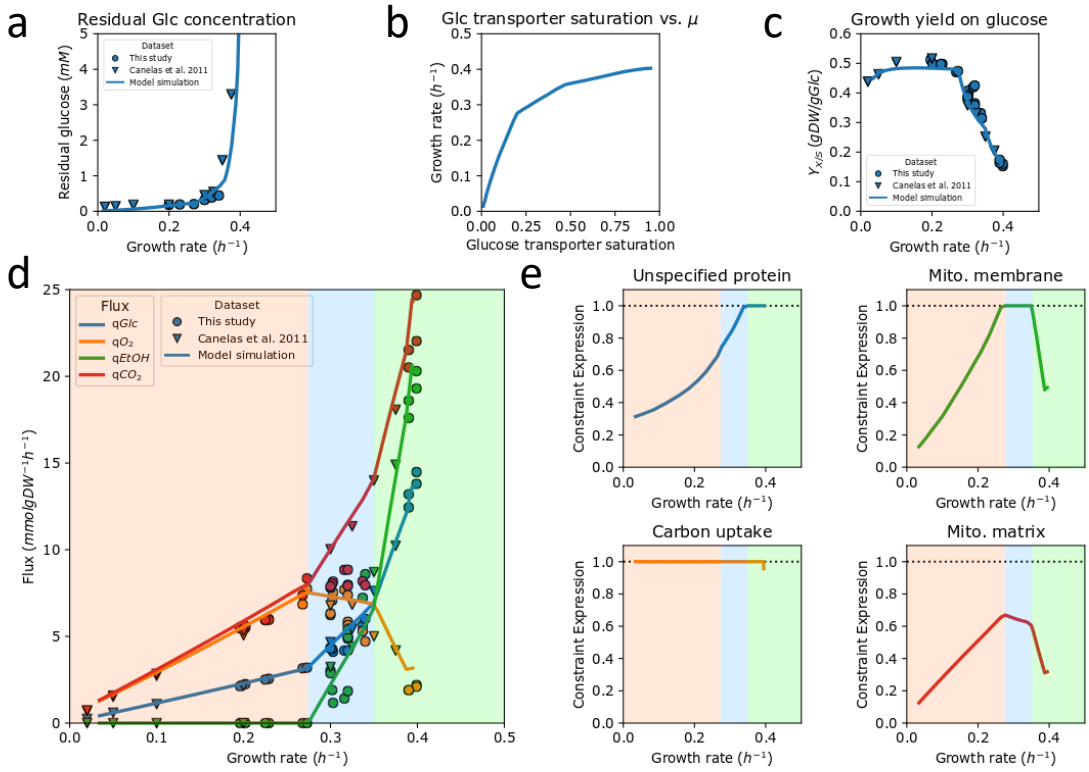

Fig. 2 Predicted and measured physiological response of *S. cerevisiae* CEN.PK as a function of glucose availability a. Measured (symbols) and predicted (line) residual glucose concentrations as a function of growth rate. The latter was calculated based on published affinity for glucose and assuming negligible intracellular glucose under these conditions. Note that this resembles a Monod growth curve but with the dependent and independent axis swapped, as we control growth rate in a chemostat. **b.** Maximal feasible growth rates of the model as a function of the glucose transporter saturation. **c.** Measured (symbols) and predicted biomass yield on glucose. **d.** Experimental fluxes from glucose-limited chemostats at different dilution rates (circles) and from two batch experiments (triangles): excess trehalose (which mimicks glucose limitation at low dilution rate[30]) and excess glucose at the highest growth rate. The lines are model predictions; background colors indicate regimes with different active constraints; **e**. Computed proteome occupancy of different constrained protein pools. A fraction of 1 means that the compartment is full with metabolically actively proteins and constrains the growth rate at that condition.

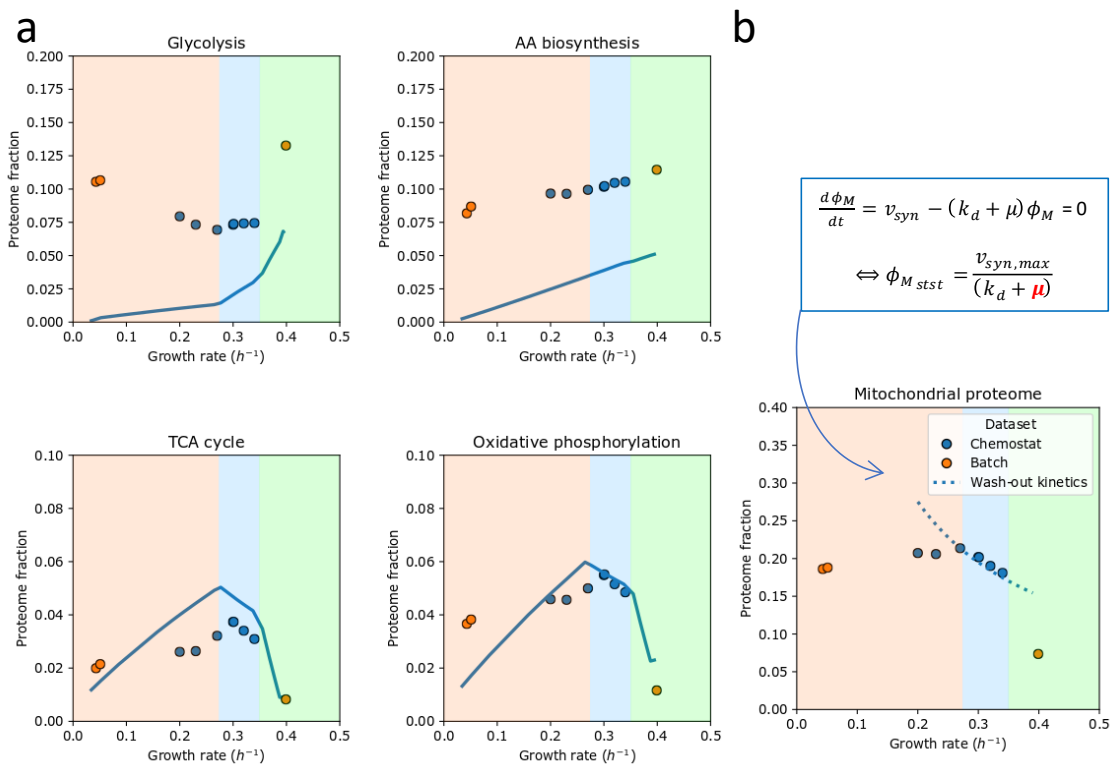

Fig. 3 Proteomics data of selected pathways as a function of glucose availability. Blue symbols are glucose-limited chemostat data; orange symbols are controlled batch experiments with excess trehalose (lowest growth rate) or glucose (highest growth rate) **a.** Comparison of predicted minimal proteome fractions to sustain growth with the experimentally determined proteome fraction for four pathways. The ratio between the two represents an estimate of the saturation level of the constituent enzymes. Lines represent the model; experimental data are symbols. **b**. Decay of steady-state mitochondrial protein fraction with growth rate at onset of ethanol formation suggests a maximal rate of mitochondrial biosynthesis $v_{syn,max}$.

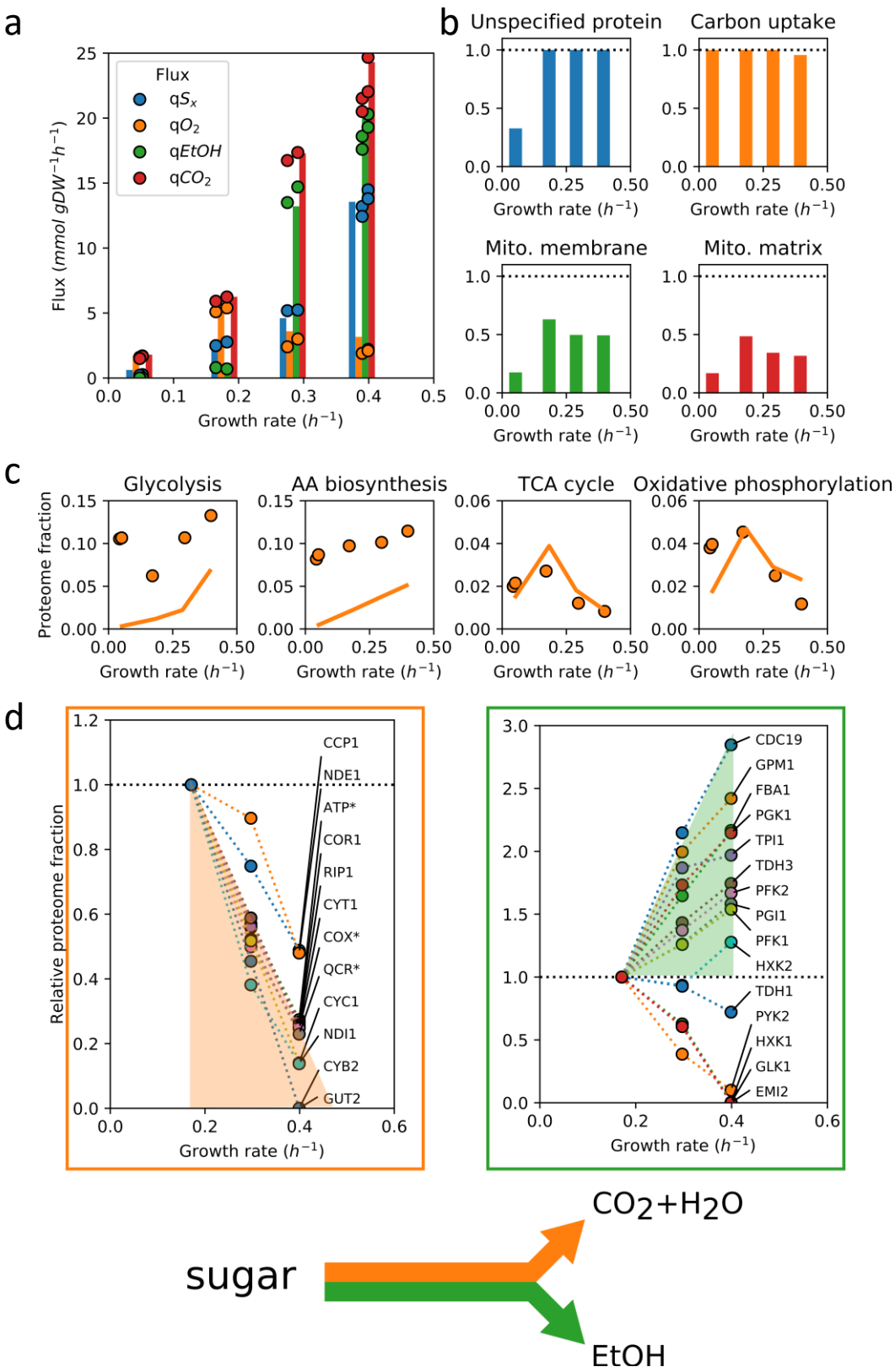

Fig. 4 Model predictions, fluxes and protein levels plotted as a function of growth rate during hexose sugar excess conditions (in the order: trehalose, galactose, maltose, glucose) a. Fluxes of sugar consumption, oxygen consumption and ethanol production. Circles are experimental data, bar plots

846 indicate model predictions (of both the growth rate and fluxes); **b**. Predicted active constraints under
847 the different sugar excess conditions as predicted by the mode (see legend of Fig. 2 for details). **c**.
848 Comparison of predicted minimally needed proteome fractions with experimentally determined ones
849 suggests differences in saturation level between pathways. Lines represent the model, experimental
850 data are circles; **d**. Linearity of the expression of individual enzymes in glycolysis (right) and respiration
851 (left) with growth rate suggests trading in of respiratory protein for fermentative protein. Asterixes
852 indicate aggregated proteome fractions instead of fractions of individual proteins. The respiratory
853 proteins converge at 0.474 ± 0.0002 h^{-1}.
854

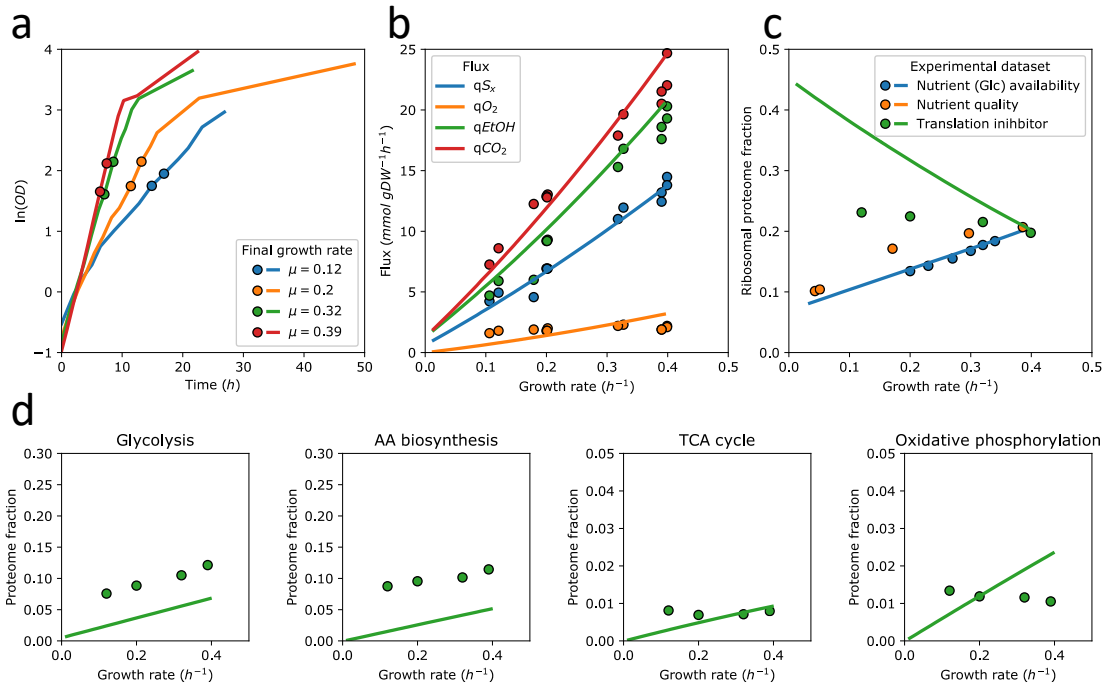

855

856 **Fig. 5 The effect of translation inhibition by cyclohexamide on growth rate, fluxes and proteome**

857 **fractions in controlled aerobic batch fermentations on glucose. a.** Dependency of culture optical density

858 (OD) on the time post-inoculation to the medium supplemented with cycloheximide. Lines are values

859 of consecutive OD measurements, points represent the times when cultures were sampled. **b-d**

860 Comparison of pcYeast predictions and experimental data: lines are model predictions; symbols are

861 experimental data points. **b**. Main catabolic fluxes as a function of the growth rate. **c**. Ribosomal

862 proteome fractions. Data from Fig. 1c are included for comparison. **d.** Proteome fractions measured

863 for key metabolic pathways, and the minimal proteome fractions predicted by pcYeast.

864

865 **Table 1.** Statistics of the pcYeast model.

Process/Compartment	# of reactions	# of proteins
Total	**24422**	**1520**
Metabolic network	**5774**	**913**
from Yeast7.6	5738	909
manually added metabolic reactions	36	4
Cytoplasm	**2349**	**778**
Plasma membrane	**529**	**114**
Mitochondria	**1089**	**272**
Endomembrane system	**2127**	**133**
Metabolic complex formation, disassembly, dilution	**2787**	**-**
tRNA turnover and modification	**2194**	**56**
Protein synthesis and turnover	**13312**	**403**
Cytoplasmic translation	1512	138
Mitochondrial translation	8	89
Protein folding	1515	31
Protein degradation	1607	42
Protein misfolding, refolding	6061	73
Protein transport	1324	30
Protein dilution by growth	1285	-
Formation of macromolecular complexes	**355**	**196**

866

867 **Table 2.** Changes to the parameters for simulating sugar excess conditions. NGAM is non-growth

868 related ATP maintenance.

Growth condition	Unit	Glucose (naïve)	Galactose	Maltose
Maximal hexose transporter area	$\mu m^2/cell$	7.5	3.0	3.5
Carbon-related NGAM	$mmol/gDW/h$	0.0	3.0	0.0
Minimal UP fraction	$g\ UP/g\ protein$	0.245	0.49	0.34

869